PAPER • OPEN ACCESS

Modulation of the thermal transport of micro-structured materials from 3D printing

View the article online for updates and enhancements.

Modulation of the thermal transport of micro-structured materials from 3D printing

Qiangsheng Sun[1]**, Zhixiang Xue**[1]**, Yang Chen**[1]**, Ruding Xia**[1]**, Jianmei Wang**[1]**, Shen Xu**[2,*]**, Jun Zhang**[1,*] **and Yanan Yue**[1,*] (ORCID)

[1] School of Power and Mechanical Engineering, Wuhan University, Wuhan 430072,
People's Republic of China
[2] School of Mechanical and Automotive Engineering, Shanghai University of Engineering Science,
Shanghai 201620, People's Republic of China

E-mail: shxu16@sues.edu.cn, zhangjun2010@whu.edu.cn and yyue@whu.edu.cn

CrossMark

Abstract

It is desirable to fabricate materials with adjustable physical properties that can be used in
different industrial applications. Since the property of a material is highly dependent on its inner
structure, the understanding of structure–property correlation is critical to the design of
engineering materials. 3D printing appears as a mature method to effectively produce
micro-structured materials. In this work, we created different stainless-steel microstructures by
adjusting the speed of 3D printing and studied the relationship between thermal property and
printing speed. Our microstructure study demonstrates that highly porous structures appear at
higher speeds, and there is a nearly linear relationship between porosity and printing speed. The
thermal conductivity of samples fabricated by different printing speeds is characterized. Then,
the correlation between porosity, thermal conductivity, and scanning speed is established. Based
on this correlation, the thermal conductivity of a sample can be predicted from its printing speed.
We fabricated a new sample at a different speed, and the thermal conductivity measurement
agrees well with the value predicted from the correlation. To explore thermal transport physics,
the effects of pore structure and temperature on the thermal performance of the printed block are
also studied. Our work demonstrates that the combination of the 3D printing technique and the
printing speed control can regulate the thermophysical properties of materials.

Keywords: modulation, thermal property, microstructure, 3D printing, speed

1. Introduction

The energy crisis has led to a growing demand for thermal
functional materials with adjustable properties according to
the requirements of thermal management and waste heat
recovery [1–6]. Furthermore, the structural complexity of
these applications prefers the flexible *in-situ* manufacturing
of these materials. Thus, the combined technique, which
could achieve both smart manufacturing and function con-
trol, is urgently desired. There are two common approaches
to adjust a material's thermophysical properties. The first
approach involves adding additional chemicals [7–9]: the
additive molecules bond with the base material and form a new
functional compound. The new bonds change the intermolecu-
lar force and may alter the properties of the original base
material to obtain the expected ones or novel physical prop-
erties. Wang *et al* [6] added La (Fe, Si)$_{13}$-based compounds

into a Cu matrix, and successfully achieved highly conductive composites with adjustable thermal expansion. Xie *et al* [2] established a fractal-intersecting sphere model to theoretically investigate the radiation feature of additive in nanoporous silica aerogels. They found that a thinner diameter of fiber and particle additives may improve the composite's insulating performance. Rai *et al* [10] studied the influence of silver (Ag) nanoparticles on the thermophysical properties and water retention of the thermal complex of polyacrylamide—Ag nanocomposites. They found that the presence of nanoparticles in the gel increases the population of bound water though H-bonding interactions, which directly modulated the nanocomposite's thermal properties.

The second approach adjusts the microstructure and organization of materials [11–13], such as surface treatment and heat treatment [14]. Li *et al* [5] studied the effect of different constitutions and various assembly structures on microstructures and properties of a silicon-based aerogel. They pointed out that composition optimization and microstructure reconstruction were the most convincing and effective strategies to improve microstructure properties for mechanical and thermal insulation. Lee *et al* [15] used the finite element method to successfully predict the porous type, or pore ratio, of ceramic composites and the change in material properties according to their detailed structure. Wang *et al* [1] analyzed the microstructural dependence of the thermal conductivity of two polycrystalline zircaloy-4 samples using extended Raman thermometry. The Kapitza thermal resistance model could account for the dependence of thermal conductivity as a function of grain size.

Additive manufacturing, commonly known as 3D printing, has strong capabilities for manufacturing complex architectures and virtual 3D objects [16, 17]. Espalin *et al* [18] proposed that devices, such as heat sinks and heat pipes, could be directly combined into t3D printed buildings, thus providing advanced thermal management of the system. Through artificially controlling the laser power, scanning speed, scan spacing, and layer thickness, 3D printing can introduce microstructural phases, such as pores [19] and microstructures, and produce an object in which each part can be assigned a different physical property.

By designing a complex microstructural assembly and specific pore distribution, one can obtain anisotropic materials [4, 20–23] and functionally graded materials (FGMs) [18, 24–27]. Hamzah *et al* [28] and Nikzad *et al* [29] added copper ferrite ($CuFe_2O_4$) as a reinforcement to print an ABS composite and achieved a 93% improvement in thermal conductivity when loaded with 14 wt% $CuFe_2O_4$. Shemelya *et al* [4], studied the effect of the composite geometry, filler morphology, and printing direction on thermal anisotropy and demonstrated that thermal conductivity can be controlled through the combination of print Raster direction and material design. Yoo *et al* [30] presented a design framework for 3D internal scaffold architectures to simultaneously match the desired mechanical properties and porosity by introducing an implicit interpolation algorithm. In addition, Pei's group [16] used 3D printing technology to produce FGMs characterized by the gradual variation in their composition and structure

over volume, resulting in corresponding changes in the material properties. They further developed a predictive model for proper process control.

In this work, 3D printing technology is used to simultaneously produce microstructures and continuously manufacture samples of variable thermal conductivity. First, steel sample blocks are produced at different scanning speeds. The microstructure, size, and distribution of the pores in the blocks are measured, and the change of porosity and the number of pores with the scanning speed are studied. Second, a noninvasive thermal measurement method based on infrared thermal imaging is developed to measure the thermal conductivity of the samples and the correlation among the thermal conductivity, porosity, and scanning speed is established. Verification of the correlation is then conducted on a newly printed sample. Moreover, the porosity and temperature effects are explored theoretically and experimentally. The result in this work demonstrates that changing the 3D printing scanning speed regulates the material structure and adjusts the physical properties of the corresponding materials.

2. Microstructure characterization and regulation

2.1. Sample preparation and structural characterization

The 304L stainless steel sample blocks were prepared using selective laser melting (SLM) technology [31–34] at different scanning speeds through an independently developed AMPRO SP-500 industrial-grade metal printing system by Suzhou Beifeng Technology Company. The 304L stainless steel powder from the aerosol method is employed to meet the requirement of high-quality powder precursors of the technology [35], which has a spherical or nearly spherical shape with good fluidity. The apparent density of the powder is greater than 4.7 g cm^{-3}, and the particle size distribution range is $15 \sim 53$ μm. The element content from the energy dispersive spectrometer study (table 1) demonstrates that the 304L stainless steel powder has an ultra-low carbon content.

Since the laser power, scanning speed, scan spacing and layer thickness are the key factors affecting the final micro structure of 3D-printed products [36], a laser volumetric energy density (VED) [37] is introduced to describe the average input energy per unit volume of the material during the SLM process.

$$\text{VED} = \frac{P}{vht} \qquad (1)$$

where P is the laser power (W), v is the scanning speed (mm s^{-1}), h is the scan spacing (μm), and t is the layer thickness (μm).

The samples are prepared using the stripes scanning strategy which is characterized by a 15 degree deflection of each scanning layer relative to the previous printing layer. This scanning strategy can effectively reduce the overlap along the laser scanning paths in adjacent layers and avoid heat accumulation and defect formation. All samples are produced in a nitrogen atmosphere and have the same geometrical dimensions ($25 \times 30 \times 5$ mm^3). The porosity of the sample

Table 1. The main composite of 304L alloy powder (wt%).

Element	Fe	Cr	Ni	Mo	Mn	Cu	Si	C
Content	Residue	20	10	1.03	2	1	1	⩽0.03

Table 2. Preparation parameters of 304L sample.

	P (W)	H (μm)	t (μm)	v (mm s^{-1})	VED (J mm^3)
S1	220	80	40	700	98.2
S2	220	80	40	900	76.3
S3	220	80	40	1100	62.5
S4	220	80	40	1300	52.9
S5	220	80	40	1500	45.8
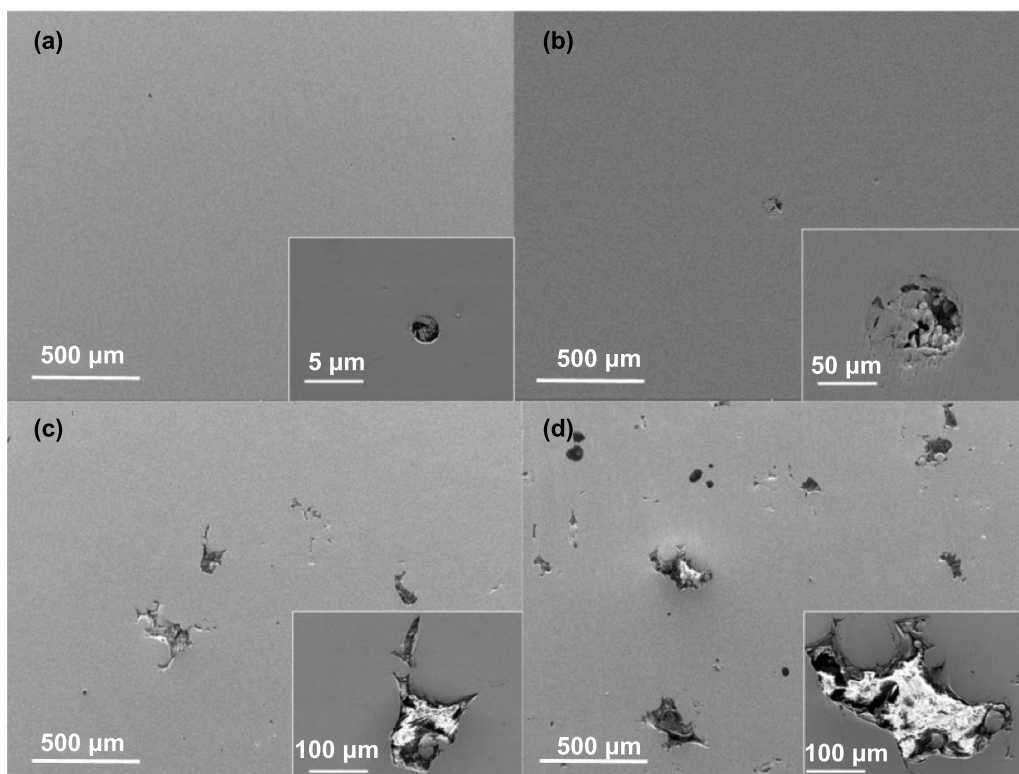
Figure 1. SEM images of the 3D-printed steel samples' surface formed by different scanning speeds of (a) 700 mm s^{-1}, (b) 900 mm s^{-1}, (c) 1100 mm s^{-1}, and (d) 1300 mm s^{-1}. (The inset shows the detail of the pore under the higher magnification.)

is varied by changing the scanning speed at a constant laser power. Table 2 lists the detailed experimental parameters for each sample.

The scanning electron microscopic (SEM) images illustrate the structure of the 304L samples with the different scanning speeds of 700, 900, 1100, and 1300 mm s^{-1}, as shown in figure 1. It is obvious that the number of pores in the sample gradually increases with the increase of scanning speed. For example, when the scanning speed is 700 mm s^{-1} (figure 1(a)), a few pores are observed in the SEM image at low magnification in figure 1(a). At the same time, its density is higher than others. At a high magnification (inset in figure 1(a)), some pores appear and show a perfectly round shape with a diameter of 5–10 μm. The round pores

formed because the molten pool captures the air contained in the powder during the melting process. However, the solubility of air decreases during the solidification process of the molten pool, and the air precipitates out to form round pores.

As the scanning speed increases from 900 to 1100 mm s^{-1}, the porosity obviously increases, and the shape of the pores gradually become larger and irregular. Figures 1(b)–(d) clearly shows that the pores contain unfused powder particles. This is because the time span decreases for the laser spot, staying on the welding path per unit length along with the faster scanning speed. The width of the molten pool also decreases because of the Gaussian distribution of the laser energy across the weld path. The center energy input of the laser can melt
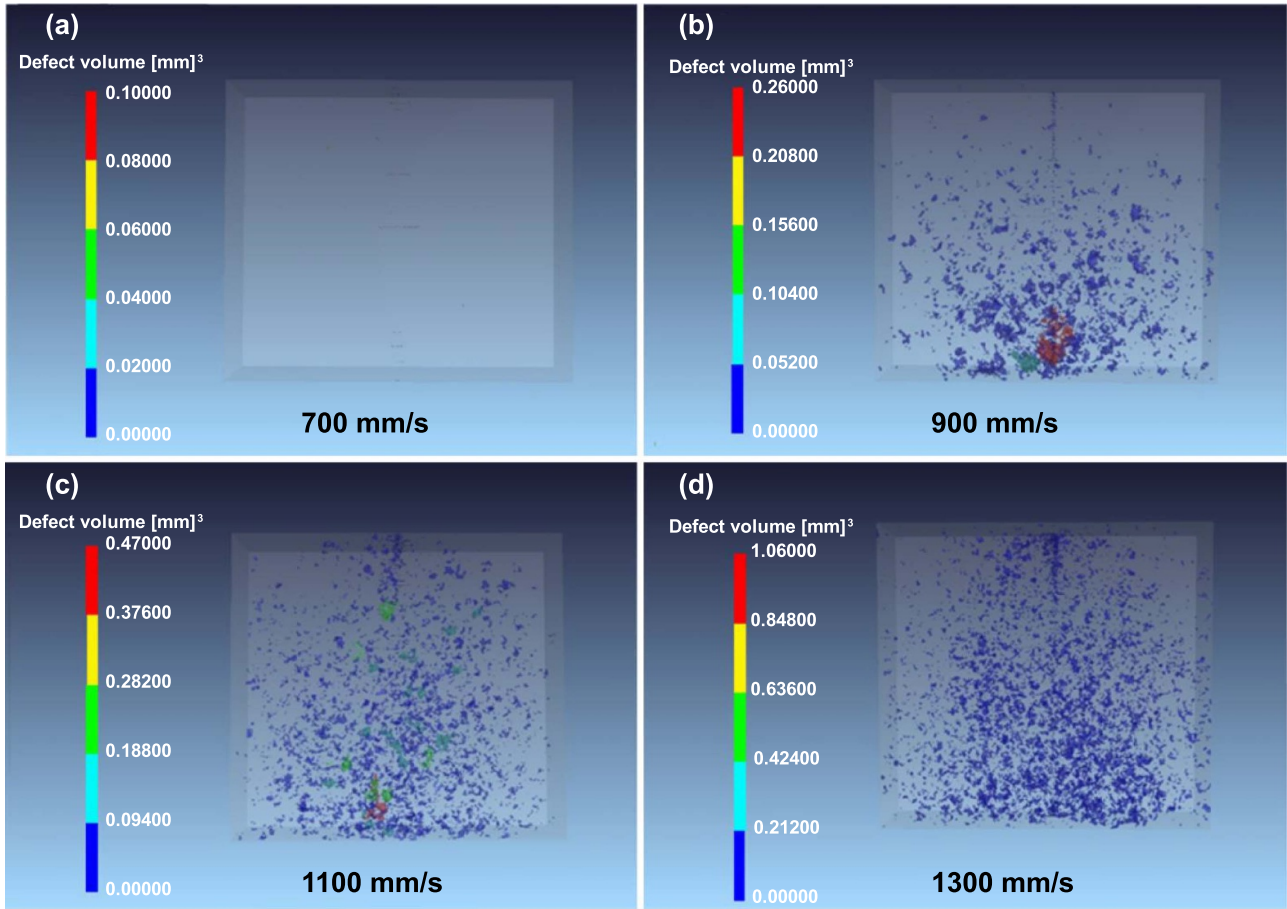
Figure 2. Micro CT image of the 3D-printed iron materials formed by different scanning speeds of (a) 700 mm s^{-1}, (b) 900 mm s^{-1}, (c) 1100 mm s^{-1}, and (d) 1300 mm s^{-1}.

the powder in the center of the molten pool, while the powder at the edge of the molten pool could not absorb enough energy to melt. It forms unfused holes in the lap joints of the molten pool [38]. Based on the same mechanism, the high scanning speed also leads to a decrease in the depth of the molten pool. Furthermore, the incompletely melted powder occurring at the interface results in poor interlayer bonding and produces non-fusion defects [39].

2.2. Microstructure regulation

The micro CT images in figure 2 show the porosity, number of pores, pore size, and pore distribution of the four samples [40]. The 3D renderings of the. 304L stainless steel samples are marked with different colors to characterize pores of different sizes, in which the blue mark represents smaller pores and the red mark represents larger surface pores. The pores with an equivalent diameter less than 50 μm are neglected in figure 2. As the laser scanning speed increases from 700 to 1300 mm s^{-1}, the pore density of the samples gradually increases. The distribution of the pores is relatively uniform, which is consistent with the SEM results. The quantity of the main micro-structure, the small pores (blue),
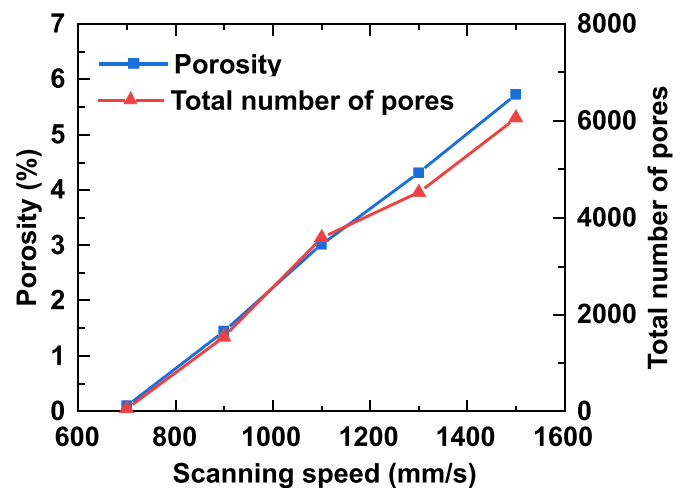

Figure 3. Characterization results of scanning speed dependent porosity and total number of pores.

increases and evenly spreads in the sample, while the number and size of the randomly occurring large pores gradually increases.
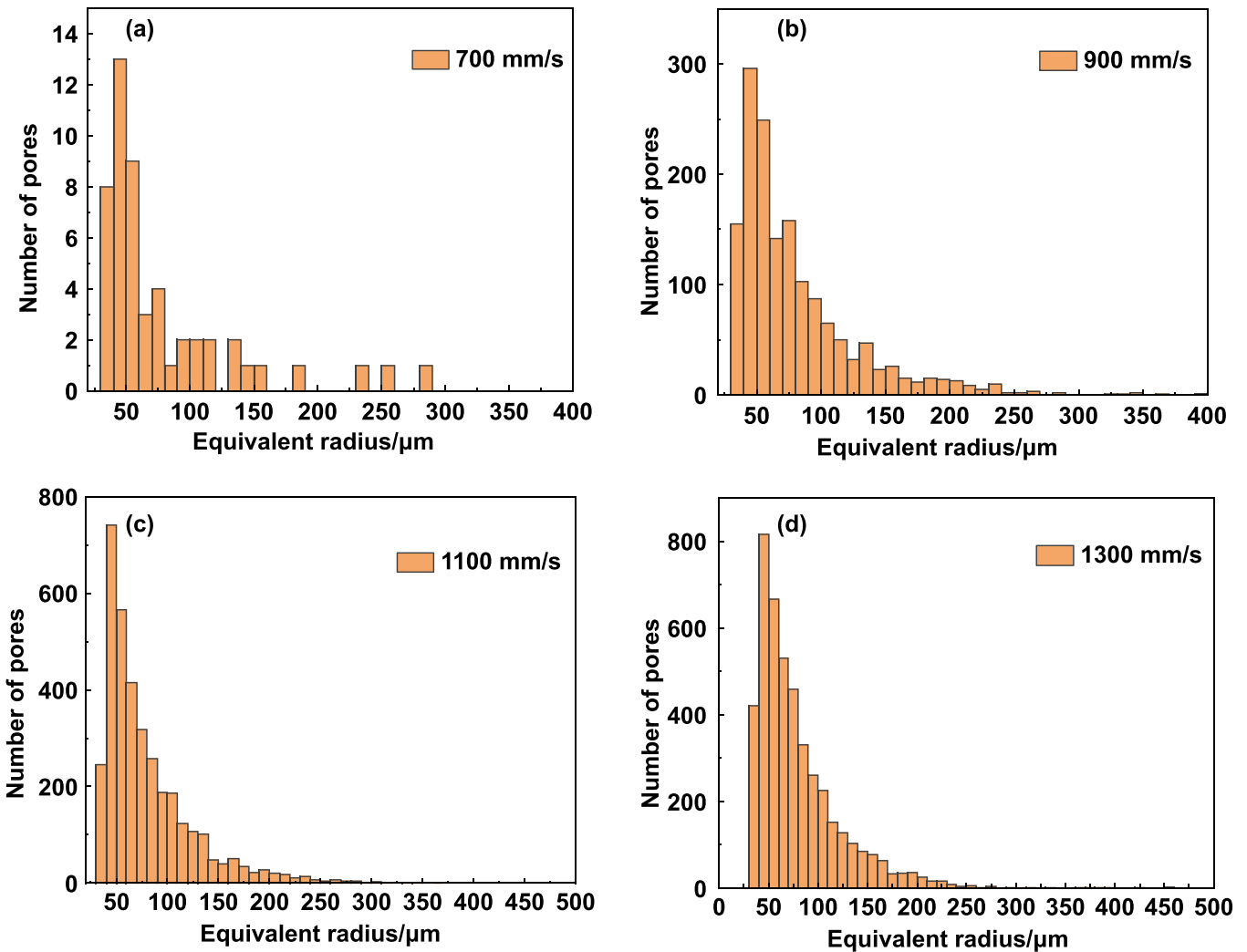
Figure 4. Pore distribution against the equivalent radius at a scanning speed of (a) 700 mm s^{-1}, (b) 900 mm s^{-1}, (c) 1100 mm s^{-1}, and (d) 1300 mm s^{-1}, respectively.

The variation of the volumetric porosity and the total number of pores against the scanning speed are shown in figure 3. Both the porosity and the total number of pores increase almost linearly against the scanning speed. When the scanning speeds are 700, 900, 1100, and 1300 mm s^{-1}, the volume porosity increases to 0.10%, 1.45%, 3.01%, and 4.31%, respectively. The total number of the pores in sample S1 is 52, while the total number increases to 4522 for sample S4.

Figure 4 shows the equivalent diameter distribution of the pores in samples S1-S4. The pore diameters scatter in a range of 0–600 μm. The maximum pore diameter also increases along with the increase in the scanning speed (figures 4(a)–(d)). The maximum equivalent pore diameter is 566, 791, 974, and 1263 μm, when the scanning speed is 700, 900, 1100, and 1300 mm s^{-1}, respectively. As the scanning speed increases, the occurrence of unfused defects leads to a flow of partially melted metal powder. In the subsequent deposition process, interlayer defects gradually expand and propagate upward, and thus form large multi-layer defects [41]. The aggregation of

small pore size is also one possible explanation for the increase in pore size [42].

3. Thermal conductivity measurement

The varying quantities of the microstructure raised by the scanning speed in the sample manufactory changes the material's thermophysical properties. Accurate knowledge of the correlation between thermal conductivity and the scanning speed is critical for predicting the thermal conductivity of these micro-structured materials, especially in the application of thermal functional structures and thermal metamaterials. Here, we develop a non-contact method for the thermal conductivity measurement, which employs a laser heating source and infrared thermal imaging.

3.1. Thermal conductivity measurement based on infrared imaging

3.1.1. Mechanism of measurement. Heat convection and heat radiation are neglected in the following analysis since
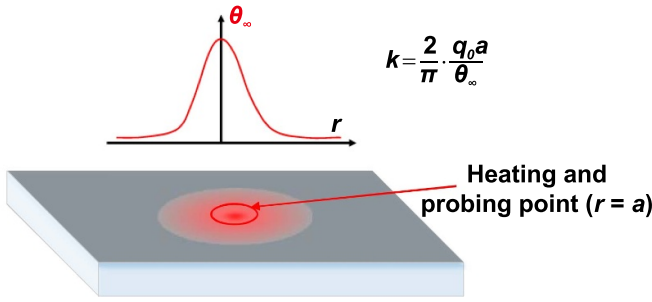
Figure 5. The mechanism of the thermal conductivity measurement method.

the thermal energy conducting through the 304L steel sample exceeds the heat loss to its surroundings. Assuming that the heating laser is a parallel beam and comes from the $-z$ direction, the physical model of heat conduction in the sample can be simplified as a semi-infinite medium with a constant heat flux in a limited region on the top of the medium. The rest of the surface has an adiabatic boundary, as shown in figure 5. The generated heat propagates along both the radial and depth direction of the medium. The governing equation is expressed as:

$$\frac{1}{r}\frac{\partial}{\partial r}\left(r\frac{\partial \theta}{\partial r}\right) + \frac{\partial^2 \theta}{\partial z^2} = \frac{1}{\alpha}\frac{\partial \theta}{\partial t}. \tag{2}$$

The boundary conditions are:

$$-k\frac{\partial \theta(r,0,t)}{\partial z} = \begin{cases} q_0 & for \quad 0 < r < a \\ 0 & for \quad r > a \end{cases}$$

$$\theta(r,z,t) \to 0 \text{ for } r \to \infty \text{ and } z \to \infty.$$

The initial condition is:

$$\theta(r,z,0) = 0$$

where, θ is the temperature rise, α is the thermal diffusivity, a is the spot radius, k is the thermal conductivity, and q_0 is the constant heat flux, $q_0 = Q_0/(\pi \cdot a^2)$. Q_0 is the heating power of the incident laser.

By solving equation (1), the temperature rise distribution on the sample surface can be obtained as shown in equation (2).

$$\frac{\theta(r,0,t)}{q_0 a/k} = \int_{\beta=0}^{\infty} erf\left[\frac{\beta(\alpha t)^{1/2}}{a}\right] J_0(\frac{\beta r}{a}) J_1(\beta) \frac{d\beta}{\beta} \tag{3}$$

where $\theta(r,0,t)$ is the temperature rise of the sample surface at time t and the location r. erf is the error function. J_0 and J_1 are the first-class Bessel functions of order 0 and order 1, respectively. The center of the area under laser irradiation ($r = 0$) has the highest temperature rise, so it is the easiest for the infrared camera to detect. Thus, after the sample surface
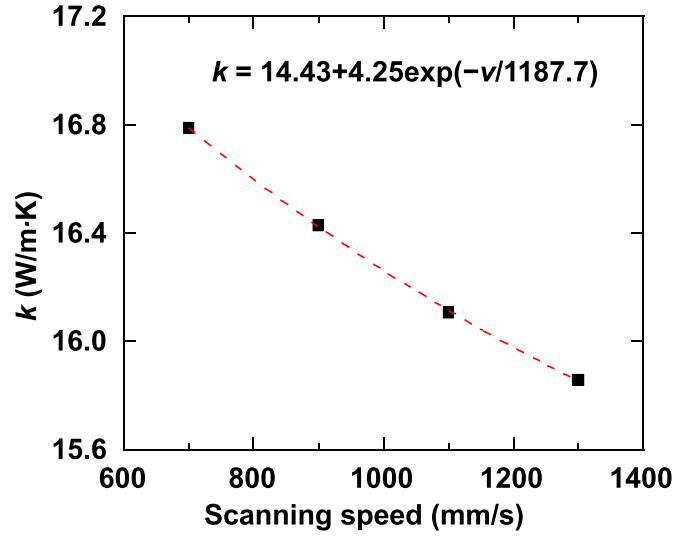

Figure 6. Characterization results of the scanning speed dependent thermal conductivity of the 304L stainless steel samples.

reaches the thermal steady state, by simplifying equation (2), k of the sample can be obtained as follows:

$$k = \frac{2}{\pi} \cdot \frac{q_0 a}{\theta_\infty} \tag{4}$$

where θ_∞ is the temperature rise at the center point after stabilization.

3.1.2. Experimental details of the thermal conductivity measurement. The experimental setup of the thermal conductivity measurement is listed as follows: a continuous-wave laser with a wavelength of 532 nm works as a heating source and is focused on the sample's surface through a convex lens. The laser spot radius measured by the blade method is $a = 0.18$ mm. Since the smooth surface of the samples is highly reflective to the incident laser, a thin black graphene coating of 8 μm thick is applied to guarantee the total absorption and surface emissivity of 0.99. The above mentioned Q_0 equals $\varepsilon \times Q$, where Q is the laser power and ε is the surface emissivity.

In the experiment, we attempt to reduce the experimental error caused by heat loss, and the temperature rise of the sample is controlled within 10 °C. Furthermore, the infrared camera remains as perpendicular to the sample surface as possible to prevent the measurement error caused by the sample's directional emissivity. The laser power is characterized by a power meter to ensure accuracy. Each measurement is repeated several times for averaging to reduce measurement uncertainty.

3.2. Correlation between thermal conductivity and scanning speed

The thermal conductivity of the samples prepared at different scanning speeds is shown in figure 6. As the laser scanning speed increases from 700 to 1300 mm s^{-1}, k of the
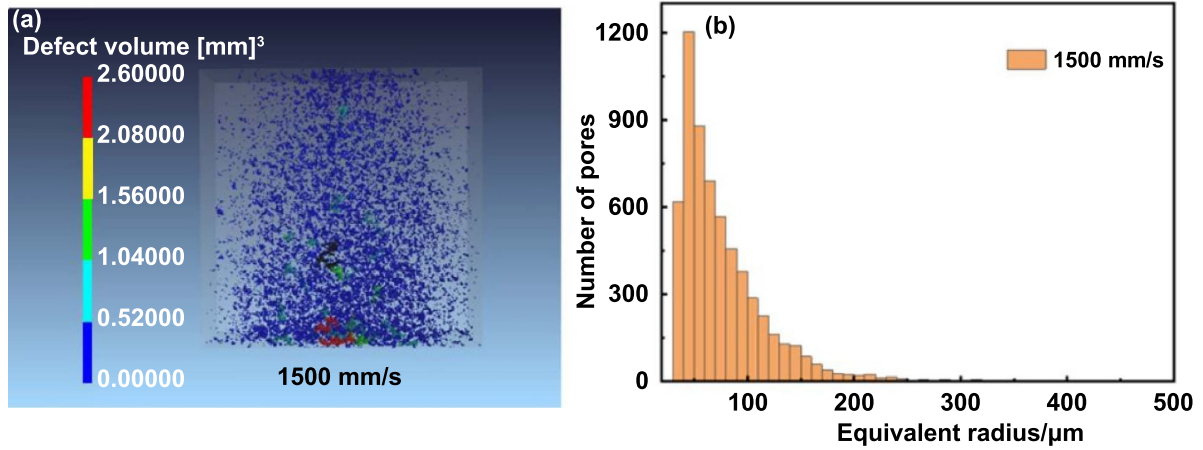
Figure 7. (a) Micro CT image of the 3D-printed iron materials formed by a scanning speed of 1500 mm s^{-1}. (b) Number of pores distributed along the equivalent radius at a scanning speed of 1500 mm s^{-1}.

304L stainless steel samples gradually decreases from 16.78 to 15.85 W (m·K)$^{-1}$, and the decreasing trend becomes smaller. The correlation between k and the scanning speed v is nonlinear fitted, and it can be expressed as:

$$k = 14.43 + 4.25e^{-\frac{v}{1187.7}}. \tag{5}$$

The different microstructures produced by the four scanning speeds may account for the variation in thermal conductivity. According to the structural characteristics of the samples at different scanning speeds, pores are the main structural cause that breaks the continuity of the samples and hinders heat conduction as they add extra boundaries along the phonon scattering path. Thus, the linear increase in the porosity and total pore number with the increment of the scanning speed lowers the thermal conductivity of the printed samples. By controlling the 3D printing scanning speed, one could artificially introduce pores to a desired content in order to manually adjust the thermal transport properties of the printouts.

3.3. Validation of thermal conductivity regulation via scanning speed control

To verify the idea of regulating the thermal properties of 3D-printed bulk by controlling the scanning speed, we then print a new sample, S5, at a set speed of 1500 mm s^{-1} using the same printing procedures and experimental conditions. Figure 7 shows the porous structure of sample S5. As expected, S5 has more pores. The total number of pores in S5 is around 6050. Most pores have a smaller size marked in blue, while the red marks increase, illustrating the appearance of larger pores. The size analysis in figure 7(b) indicates that the size distribution of the pore is similar to the previous samples, ranging between 0 and 600 μm, and the maximum equivalent radius of the pores is 852 μm.

Given the set speed of 1500 mm s^{-1}, the expected k of the sample should be 15.63 W (m·K)$^{-1}$ according to the correlation in equation (4). Our experimental measurement determines that k of sample S5 is 15.62 W (m·K)$^{-1}$. The difference of 0.6% between the estimated value and the true value

substantiates the effectiveness of the correlation between the thermal conductivity and the scanning speed. This validation also indicates the potential application of controlling the scanning speed in the 3D printing technique to regulate the thermal properties of the printed products to meet real demand.

4. Effects of porosity and temperature on thermal properties

4.1. Porosity effect

Porosity affects the overall thermal conductivity of porous materials. To deeply explore the heat transfer mechanism inside the porous stainless-steel samples, the 3D block is simplified into a 2D model, and the steady numerical model is implemented in COMSOL, shown in figure 8(a).

The computation domain is a square area where circles are evenly distributed. In the domain, the circular region represents an air pore with a typical radius r of 0.05 mm. According to the micro CT results, the remaining area is a steel base. The size of the calculation domain is set as $Lx \times Ly = 25 \times 25$ mm. For the solid region, heat transfer can be considered as steady-state heat conduction, and the governing equation is as follows:

$$\lambda_s \cdot \nabla^2 T = 0 \tag{6}$$

where λ_s is the steel's thermal conductivity.

For the fluid region, the air flow can be considered as steady laminar natural convection, and the conservation equations of mass, momentum and energy are as follows:

$$\nabla^2 \cdot \vec{V} = 0 \tag{7}$$

$$\vec{\nu} \cdot \nabla \vec{\nu} = -\frac{1}{\rho_g} \nabla p + v_g \nabla^2 \vec{\nu} + \beta(T - T_0)g \tag{8}$$

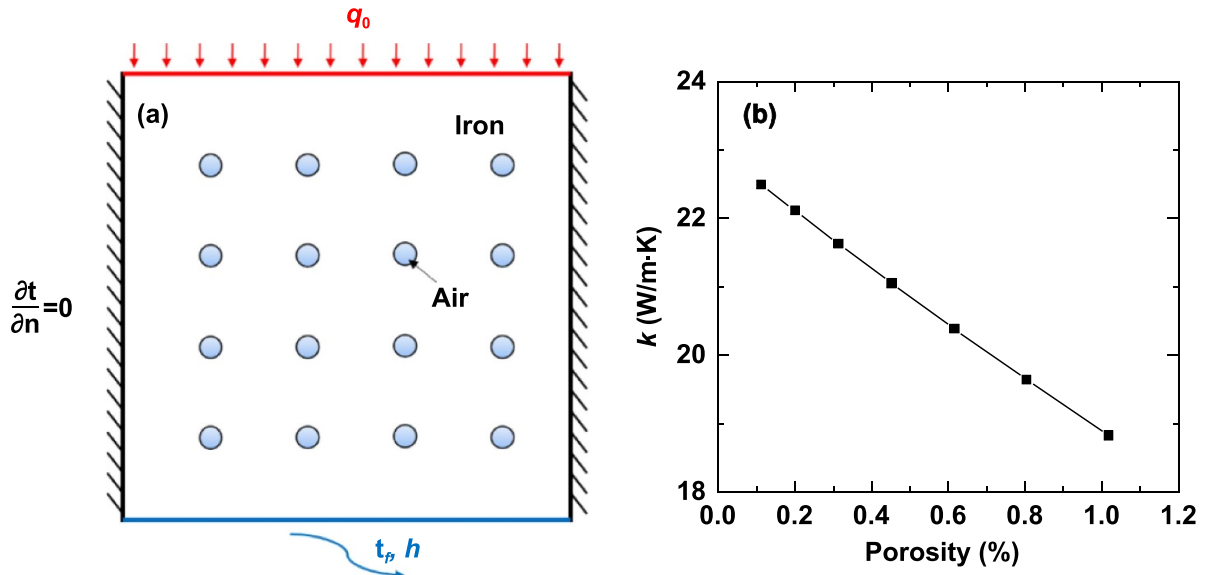$$\rho_g C_p(\vec{\nu} \cdot \nabla T) + \nabla q = 0 \tag{9}$$

Figure 8. (a) Schematic of the studied configuration. (b) The results of porosity dependent thermal conductivity of 3D-printed iron materials.

$$q = -\lambda_g \nabla T + q_r. \qquad (10)$$

Raptis *et al* [43] and Mahmoud [44] use the Rosseland approximation for thermal radiation and apply it to optically thick media to calculate the radiative heat flux:

$$q_r = -\frac{4\sigma}{3\beta_R} \nabla T^4 \approx -\frac{16T^3\sigma}{3\beta_R} \nabla T \qquad (11)$$

where $\vec{V}, T, p, \rho_g, \upsilon_g$, and β are the velocity vector, temperature, pressure, air density, the kinetic viscosity of air, and the volumetric expansion coefficient of air. g is the gravity. λ_g is the thermal conductivity of air. β_R is the Rosseland average extinction coefficient, and σ is the Stefan–Boltzmann constant.

There is a no-slip boundary condition on all of the solid-gas interfaces; the left and right boundary is the adiabatic boundary $(\partial T / \partial n = 0)$. The upper boundary is set as a heat source with an input heat flux of 100 W m^{-2}. A convection boundary of $-\lambda_s \cdot \partial T / \partial n = h(T - T_f)$ is applied to the lower boundary with a convective heat transfer coefficient of 10 W (m^2·K)$^{-1}$. The simulated k in figure 8(b) shows that it decreases nonlinearly from 22.49 to 18.82 W (m·K)$^{-1}$, when the porosity increases from 0.11% to 1.02%. It is consistent with the experiment results.

In addition to porosity, the heat transfer mechanism in the pore also affects the sample's overall thermal conductivity. This section explores the heat transfer mechanism in a single air pore, including heat convection, radiation, and heat conduction in the pore, respectively [45]. A 2D schematic diagram of a single-pore structure model is shown in figure 9. The simulation domain ($Lx \times Ly = 0.1 \times 0.1$ mm) contains only one pore with a radius r of 0.05 mm based on the Micro CT result. The inside of pore is filled with air, and the domain outside of the pore is steel. As for the solid region, the heat transfer can be considered steady heat conduction, and the governing
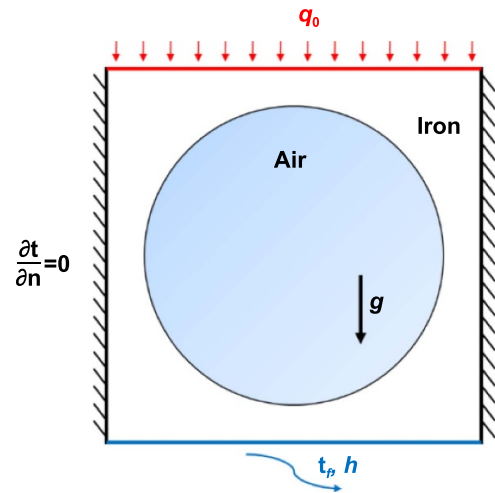
equation is shown in equation (5). For the fluid region, the conservation equations of mass, momentum and energy are shown in equations (6)–(10). The boundary conditions are set as follows: the left and right boundaries are adiabatic, the upper boundary is set as a heat source with a heat flux of 500 W m^{-2}, and the lower boundary is a convective heat transfer boundary. The convective heat transfer coefficient is 10 W (m^2·K)$^{-1}$. Heat diffuses from top to bottom in the domain, and finally the domain reaches a thermally steady state. All involved thermal properties are assumed to be constant.

Figure 10 shows the simulated results, including the temperature distribution, radiation field, velocity field, and streamline in the air domain. The concave isotherm in the pore area in figure 10(a) illustrates that heat is mainly conducted along the steel [46, 47] substrate due to the combined effects of the steel domain's high thermal conductivity and the air domain's high

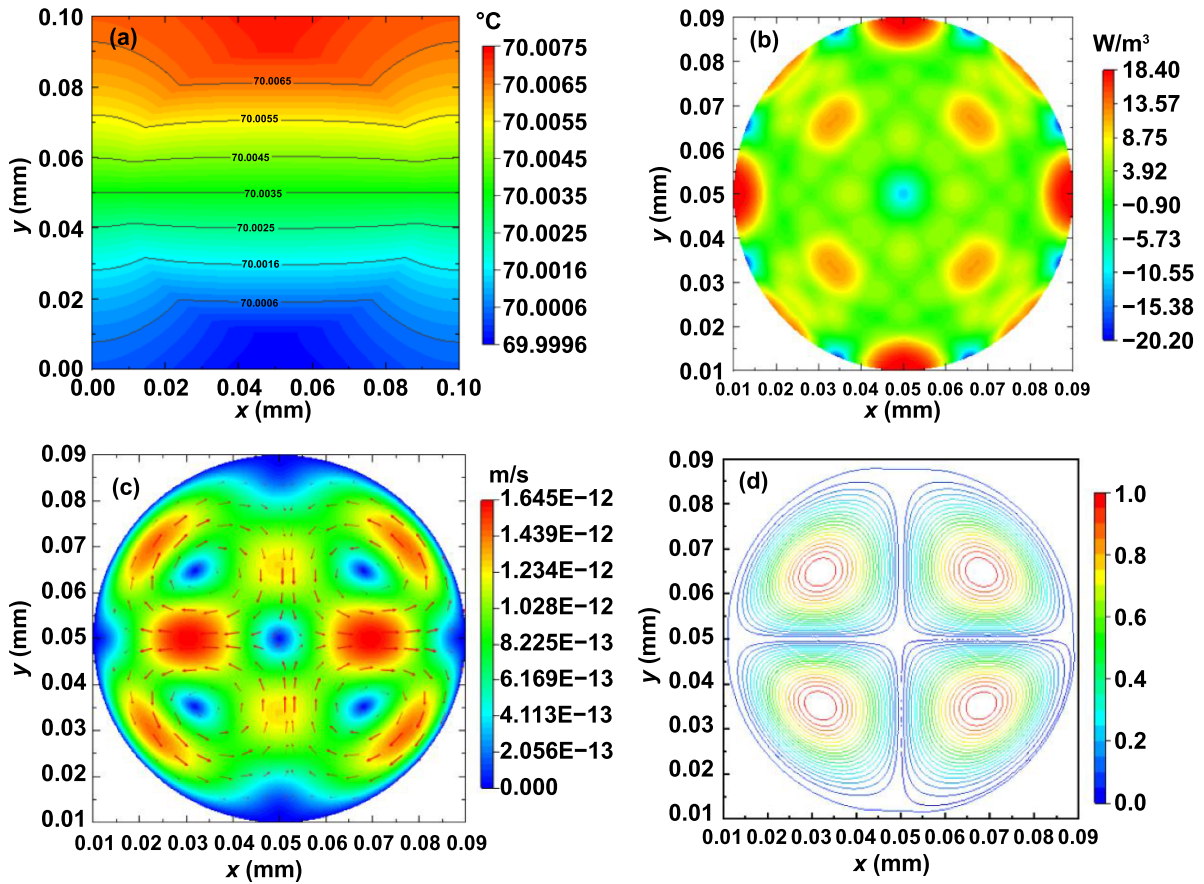**Figure 9.** Schematic of the studied single-pore configuration.

Figure 10. Thermal simulation of the single pore configuration. (a) Temperature field and isotherm. (b) Radiation field. (c) Velocity field and flow direction. (d) Streamline.
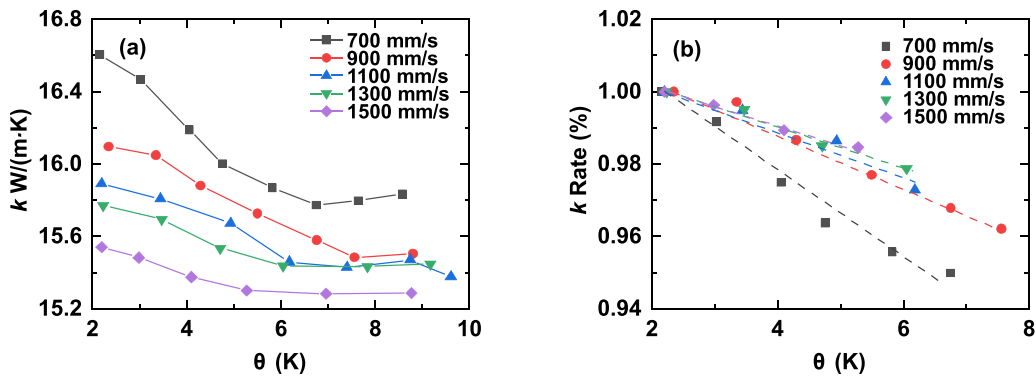

Figure 11. (a) Thermal conductivity and changing rate (b) at different scanning speeds with various temperature rise. Dashed lines in figure b show the changing trend.

thermal resistance. Thus, the temperature difference around the single micro-sized pore is small. Figure 10(b) shows the symmetrical radiation intensity in the air pore, proving that the radiation heat transfer in the closed cavity equalizes the temperature distribution [48]. Both the velocity field and streamline in figures 10(c) and (d) exhibit the feature of a vortex. Four symmetrically distributed circulations form. This is because the steel structure has a large thermal conductivity. The temperature increases at a much higher rate than the air in the pore, and the hot wall heats the adjacent air immediately after its

temperature rises. As a result, the hot air flows upward due to the decreasing density and gathers at the top of the cavity. The accumulation of air molecules results in a density increment and causes the air to decline and turn towards the left and right walls. When the air flow reaches the left and right walls, it is pushed toward the heat source and heated up again. This repeated cycle forms the vortex [49]. The large value of the streamline indicates a strong vortex and high fluid velocity. As shown in figure 10(d), a region of higher velocity forms on the wall and the transverse central axis.

4.2. Temperature effect

Temperature is another important factor that affects the overall thermal conductivity of materials in application. The samples are heated up to different temperatures to explore the variation in their thermal conductivity. Based on equation (3), the curves of the heating power against temperature rise are plotted, and the thermal conductivity is the first derivative of the curves in figure 11(a). In the low temperature rise range (0 °C–5 °C), the thermal conductivity for all of the samples decreases as the temperature increases. It appears that the steel base dominates the heat conduction in the sample. A metal's heat conduction mainly depends on the electron heat conduction [50]. When the temperature rises, the thermal motion speed of electrons increases the collision between electrons and the lattice is frequent, and the average free path is accordingly shortened, so the thermal conductivity drops. However, when the temperature rise is higher than 5 °C, the heat convection at the heating point becomes large and affects the measured thermal conductivity. Thus, it is difficult to observe the decreasing trend of thermal conductivity against temperature. The changing percentage of the thermal conductivity in figure 11(b) shows that the thermal conductivity of the sample containing more pores decreases more slowly against the temperature.

5. Conclusion

In this work, micropore-structured stainless-steel blocks were produced using 3D printing technology at different scanning speeds: 700, 900, 1100, and 1300 mm s^{-1}. Structure characterization illustrated that the maximum equivalent diameter and the number of the pores increased with the scanning speed, while the distribution remained uniform in all of the sample blocks. The volumetric porosity increased linearly against the scanning speed. Based on this observation, we further measured the thermal conductivity of the sample blocks. As the laser scanning speed gradually increased from 700 to 1300 mm s^{-1}, the thermal conductivity of the samples nonlinearly decreased from 16.78 to 15.85 W (m·K)$^{-1}$. The decreasing trend can be expressed as $k = 14.43 + 4.25^{-v/1187.7}$. With this correlation, the thermal conductivity of a new sample produced with a scanning speed of 1500 mm s^{-1} was predicted and verified. The small difference of 0.6% proves that controlling the 3D printing scanning speed regulate the thermal conductivity of the products. Numerical simulation was conducted to investigate the heat transfer process in the porous block and the single pore structure. The temperature effect on the thermal conductivity of the printed samples was studied. The thermal conductivity decreased with the increase of temperature and the rate of decrease was measured. In summary, the regulation of the microstructure and thermal conductivity of the printed blocks was achieved by controlling the scanning speed in the 3D printing process.

Acknowledgments

ORCID iD

Yanan Yue https://orcid.org/0000-0002-3489-3949

References

[1] Wang H, Thomas J, Okuniewski M A and Tomar V 2020 Microstructure dependent thermal conductivity measurement of Zircaloy-4 using an extended Raman thermometry method *J. Nucl. Mater.* **539** 152338

[2] Xie T, He Y L and Hu Z J 2013 Theoretical study on thermal conductivities of silica aerogel composite insulating material *Int. J. Heat Mass Transfer* **58** 540–52

[3] Zaldivar R J, Witkin D B, Mclouth T, Patel D N, Schmitt K and Nokes J P 2017 Influence of processing and orientation print effects on the mechanical and thermal behavior of 3D-printed ULTEM® 9085 material *Addit. Manuf.* **13** 71–80

[4] Shemelya C *et al* 2017 Anisotropy of thermal conductivity in 3D printed polymer matrix composites for space based cube satellites *Addit. Manuf.* **16** 186–96

[5] Li C D *et al* 2021 A review of silicon-based aerogel thermal insulation materials: performance optimization through composition and microstructure *J. Non-Cryst. Solids* **553** 120517

[6] Xie Y S, Han M, Wang R D, Zobeiri H, Deng X, Zhang P X and Wang X W 2019 Graphene aerogel based bolometer for ultrasensitive sensing from ultraviolet to far-infrared *ACS Nano* **13** 5385–96

[7] Rani R, Juneja J K, Singh S, Prakash C and Raina K K 2013 Structural, electrical, magnetic and magnetoelectric properties of composites *J. Magn. Magn. Mater.* **345** 55–59

[8] Zhao X W, Zang C G, Ma Q K, Wen Y Q and Jiao Q J 2016 Thermal and electrical properties of composites based on (3-mercaptopropyl) trimethoxysilane- and Cu-coated carbon fiber and silicone rubber *J. Mater. Sci.* **51** 4088–95

[9] Begley M R, Gianola D S and Ray T R 2019 Bridging functional nanocomposites to robust macroscale devices *Science* **364** 6447

[10] Rai T, Sharma A and Panda D 2017 Quantifying the role of silver nanoparticles in the modulation of the thermal energy storage properties of PAM–Ag nanocomposites *New J. Chem.* **41** 2029–36

[11] Dash C and Bisoyi D K 2020 A study on the structure-property relationship of microwave irradiated sunn hemp fiber reinforced polymer composite *IOP Conf. Ser. Mater. Sci. Eng.* **798** 012015

[12] Haleshappa D, Jayarama A and Patil P S 2021 Structure and property relationship of methoxy substituted novel organic crystals for photonic applications *Mater. Today Proc.* **35** 366–73

[13] Al-Faouri T, Buguis F L, Soldouz S A, Sarycheva O V, Hussein B A, Mahmood R and Koivisto B D 2020 Exploring structure-property relationships in a bio-inspired family of bipodal and electronically-coupled *Bis* triphenylamine dyes for dye-sensitized solar cell applications *Molecules* **25** 2260

[14] Andrade-Campos A 2010 The influence of the material heat treatment and phase transformations in forming processes *Int. J. Mater. Form.* **3** 1139–42

[15] Lee D G, Kim S H, Kim S, Yu J H and Cho S W 2019 Prediction of material properties of ceramic composite

material by porous structure and porosity using the finite element method *Int. J. Precis. Eng. Manuf.* **20** 805–14

[16] Pei E, Loh G H, Harrison D, De Amorim Almeida H, Verona M D M and Paz R 2017 A study of 4D printing and functionally graded additive manufacturing *Assem. Autom.* **37** 147–53

[17] Khoo Z X, Teoh J E M, Liu Y, Chua C K, Yang S F, An J, Leong K F and Yeong W Y 2015 3D printing of smart materials: a review on recent progresses in 4D printing *Virtual Phys. Prototyp.* **10** 103–22

[18] Espalin D, Muse D W, Macdonald E and Wicker R B 2014 3D printing multifunctionality: structures with electronics *Int. J. Adv. Manuf. Technol.* **72** 963–78

[19] Kurt A and Ates H 2007 Effect of porosty on thermal conductivity of powder metal materials *Mater. Des.* **28** 230–3

[20] Ren L Q, Song Z Y, Liu H L, Han Q H, Zhao C, Derby B, Liu Q P and Ren L 2018 3D printing of materials with spatially non-linearly varying properties *Mater. Des.* **156** 470–9

[21] Nam Y J, Hwang Y K, Park J W and Lim Y M 2019 Feasibility study to control fiber distribution for enhancement of composite properties via three-dimensional printing *Mech. Adv. Mater. Struct.* **26** 465–9

[22] Dijkshoorn A, Schouten M, Wolterink G, Sanders R, Stramigioli S and Krijnen G 2020 Characterizing the electrical properties of anisotropic, 3D-printed conductive sheets for sensor applications *IEEE Sens. J.* **20** 14218–27

[23] Chen Q, Mangadlao J D, Wallat J, Leon A D, Pokorski J K and Advincula R C 2017 3D printing biocompatible polyurethane/poly(lactic acid)/graphene oxide nanocomposites: anisotropic properties *ACS Appl. Mater. Interfaces* **9** 4015

[24] Capasso I, Liguori B, Verdolotti L, Caputo D, Lavorgna M and Tervoort E 2020 Process strategy to fabricate a hierarchical porosity gradient in diatomite-based foams by 3D printing *Sci. Rep.* **10** 612

[25] Jiang P, Ji Z Y, Wang X L and Zhou F 2020 Surface functionalization—a new functional dimension added to 3D printing *J. Mater. Chem.* C **8** 12380–411

[26] Haring A P, Khan A U, Liu G L and Johnson B N 2017 3D printed functionally graded plasmonic constructs *Adv. Opt. Mater.* **5** 1700367

[27] Wang J L, Mubarak S, Dhamodharan D, Divakaran N, Wu L X and Zhang X 2020 Fabrication of thermoplastic functionally gradient composite parts with anisotropic thermal conductive properties based on multicomponent fused deposition modeling 3D printing *Compos. Commun.* **19** 142–6

[28] Hamzah K A, Yeoh C K, Noor M M, Teh P L, Aw Y Y, Sazali S A and Wan Ibrahim W M A 2019 Mechanical properties and thermal and electrical conductivity of 3D printed ABS-copper ferrite composites via 3D printing technique *J. Thermoplast. Compos. Mater.* 089270571986940

[29] Nikzad M, Masood S H and Sbarski I 2011 Thermo-mechanical properties of a highly filled polymeric composites for fused deposition modeling *Mater. Des.* **32** 3448–56

[30] Yoo D J 2014 Advanced porous scaffold design using multi-void triply periodic minimal surface models with high surface area to volume ratios *Int. J. Precis. Eng. Manuf.* **15** 1657–66

[31] Aggarwal A, Patel S and Kumar A 2019 Selective laser melting of 316L stainless steel: physics of melting mode transition and its influence on microstructural and mechanical behavior *JOM* **71** 1105–16

[32] Almangour B, Grzesiak D, Cheng J Q and Ertas Y 2018 Thermal behavior of the molten pool, microstructural evolution, and tribological performance during selective laser melting of TiC/316L stainless steel nanocomposites: experimental and simulation methods *J. Mater. Process. Technol.* **257** 288–301

[33] Guo P, Zou B, Huang C Z and Gao H B 2017 Study on microstructure, mechanical properties and machinability of efficiently additive manufactured AISI 316L stainless steel by high-power direct laser deposition *J. Mater. Process. Technol.* **240** 12–22

[34] Liu Y D, Zhang M, Shi W T, Ma Y Y and Yang J 2021 Study on performance optimization of 316L stainless steel parts by high-efficiency selective laser melting *Opt. Laser Technol.* **138** 106872

[35] Li R, Shi Y, Wang Z, Wang L, Liu J and Jiang W 2010 Densification behavior of gas and water atomized 316L stainless steel powder during selective laser melting *Appl. Surf. Sci.* **256** 4350–6

[36] Shipley H, McDonnell D, Culleton M, Coull R, Lupoi R, O'Donnell G and Trimble D 2018 Optimisation of process parameters to address fundamental challenges during selective laser melting of Ti-6Al-4V: a review *Int. J. Mach. Tools Manuf.* **128** 1–20

[37] Liu S, Li H, Qin C, Zong R and Fang X 2020 The effect of energy density on texture and mechanical anisotropy in selective laser melted Inconel 718 *Mater. Design* **191** 108642

[38] Qi T, Zhu H H, Zhang H, Yin J, Ke L D and Zeng X Y 2017 Selective laser melting of Al7050 powder: melting mode transition and comparison of the characteristics between the keyhole and conduction mode *Mater. Des.* **135** 257–66

[39] Zhang B, Li Y T and Bai Q 2017 Defect formation mechanisms in selective laser melting: a review *Chin. J. Mech. Eng.* **30** 515–27

[40] De Terris T, Andreau O, Peyre P, Adamski F, Koutiri I, Gorny C and Dupuy C 2019 Optimization and comparison of porosity rate measurement methods of selective laser melted metallic parts *Addit. Manuf.* **28** 802–13

[41] Yang K V, Rometsch P, Jarvis T, Rao J, Cao S, Davies C and Wu X H 2018 Porosity formation mechanisms and fatigue response in Al-Si-Mg alloys made by selective laser melting *Mater. Sci. Eng.* A **712** 166–74

[42] Weingarten C, Buchbinder D, Pirch N, Meiners W, Wissenbach K and Poprawe R 2015 Formation and reduction of hydrogen porosity during selective laser melting of AlSi10Mg *J. Mater. Process. Technol.* **221** 112–20

[43] Raptis A, Perdikis C and Takhar H 2004 Effect of thermal radiation on MHD flow *Appl. Math. Comput.* **153** 645–9

[44] Mahmoud M A A 2007 Thermal radiation effects on MHD flow of a micropolar fluid over a stretching surface with variable thermal conductivity *Phys. A: Stat. Mech. Appl.* **375** 401–10

[45] Saravanan S and Sivaraj C 2013 Coupled thermal radiation and natural convection heat transfer in a cavity with a heated plate inside *Int. J. Heat Fluid Flow* **40** 54–64

[46] Benyahia N, Aksouh M, Mataoui A and Oztop H F 2020 Coupling turbulent natural convection-radiation-conduction in differentially heated cavity with high aspect ratio *Int. J. Therm. Sci.* **158** 106518

[47] Anishchenko L M and Brekhovskikh V F 1974 Mechanism of heat conduction in porous metallic materials *Sov. Powder Metall. Met. Ceram.* **13** 298–300

[48] Miles A and Bessaïh R 2021 Heat transfer and entropy generation analysis of three-dimensional nanofluids flow in a cylindrical annulus filled with porous media *Int. Commun. Heat Mass Transfer* **124** 105240

[49] Venkatadri K, Bég O A, Rajarajeswari P and Prasad V R 2020 Numerical simulation of thermal radiation influence on natural convection in a trapezoidal enclosure: heat flow visualization through energy flux vectors *Int. J. Mech. Sci.* **171** 105391

[50] Ordonez-Miranda J, Alvarado-Gil J J and Yang R G 2011 The effect of the electron-phonon coupling on the effective thermal conductivity of metal-nonmetal multilayers *J. Appl. Phys.* **109** 094310